

High-efficiency scattering probe design for s-polarized near-field microscopy

Richard Ren¹ , Xinzhong Chen¹ , and Mengkun Liu^{1,2*}

¹Department of Physics and Astronomy, Stony Brook University, Stony Brook, New York 11794, United States of America

²National Synchrotron Light Source II, Brookhaven National Laboratory, Upton, New York 11973, United States of America

*E-mail: mengkun.liu@stonybrook.edu

Received December 12, 2020; accepted December 27, 2020; published online January 12, 2021

In a conventional scattering-type scanning near-field optical microscopy setup, the atomic force microscope probe is unable to effectively couple with s-polarized light, resulting in low signal and limited in-plane sensitivity. This study aims to investigate a high-resolution probe with enhanced responsivity to both s- and p-polarized light. Full-wave electromagnetic method of moments simulations are utilized. Simulated near-field spectra on prototypical materials (SiO₂, Si, SrTiO₃), as well as simulated raster scans of a gap nanoantenna, indicate a two order of magnitude increase of the scattering signal for s-polarized incident and detection scheme compared to the conventional probe.

© 2021 The Japan Society of Applied Physics

Supplementary material for this article is available [online](#)

Scattering-type scanning near-field optical microscopy (s-SNOM) has been widely used to overcome the diffraction limit in conventional optical microscopy and achieve a spatial resolution below 10 nm at infrared (IR) photon frequencies.^{1,2)} The significantly improved spatial resolution is achieved by coupling far-field incident light to an atomic force microscope (AFM) tip and probing the near-field interaction between the tip and sample via evanescent wave excitation. The electric field under the probe apex is enhanced by a few orders of magnitude because of the lightning-rod effect.^{3,4)} The scattered light from the probe carries local sample information due to complex probe-sample interactions. It has been demonstrated that the spatial resolution in the order of 10 nm depends on the probe apex radius instead of the free-space wavelength.⁵⁾ In a conventional s-SNOM setup, p-polarized light is often used. This is because when the electric field component is parallel to the probe axis, the antenna response can be maximally excited, yielding a stronger probe scattering. However, in many cases, s-polarization is preferred. For example, the resonances of certain in-plane phonon modes, plasmonic antennas, or planar metamaterials can only be excited by s-polarized light.^{6–8)} Practically, when s-polarized light is utilized with commercial AFM probes, the scattering signal as well as the signal-to-noise ratio is drastically worse.

The purpose of this paper is to design and numerically test a desired AFM probe that is capable of enhancing the response to s-polarized incident light while keeping the efficient coupling to p-polarized light. Utilizing rigorous numerical techniques, we aim to simulate spatial electric field distribution, broadband near-field spectroscopy, and monochromatic near-field imaging, as well as the directivity emission pattern of the designed probe. We demonstrate that the designed probe has an over two orders of magnitude increase in signal compared to the conventional AFM probe for s-polarized incident light.

Numerous analytical models have been developed to capture the near-field response of the probe-sample junction in s-SNOM. Among analytical models, the probe geometry is usually simplified to a sphere,⁹⁾ elongated spheroid,^{10–12)} or truncated cone.¹³⁾ However, due to the complex geometry of the real probe, analytically calculating the full electrodynamic response is deemed impractical. Therefore, full-wave numerical simulation with flexible three-dimensional modeling is desirable. Popular numerical techniques such as the finite

element method (FEM) and the finite-difference time-domain (FDTD) method have been employed to study the tip-sample near-field interactions in several studies.^{14–17)} However, given the nature of this problem where a large portion of the simulation space is free space, volume-mesh-based techniques like FEM and FDTD are less efficient compared to surface-mesh-based techniques such as the method of moments.^{18,19)} Therefore, in this study, the method of moments solver (Altair FEKO) is used to simulate the full electrodynamic response of the designed probe as well as the current probe. Previous research using a similar approach has demonstrated the quantitative simulation of tip scattering.²⁰⁾

We outline the general simulation settings. The probe is modeled as a perfect electric conductor (PEC). Even though real probes are typically made of metal-coated Si, previous studies have shown that modeling the probes as PEC yields practically no difference in results but significantly saves simulation time.^{17,20)} The sample is modeled as a semi-infinite half-space with the tip-sample interaction calculated using exact Sommerfeld integrals. No cantilever was simulated because it has an insignificant effect on the near-field interaction of the probe and the sample.²⁰⁾ To evaluate both the designed and conventional AFM probes in a realistic experimental setting, this tip was illuminated with an incident plane wave at $\theta = 60^\circ$ incident angle of variable wavelength and polarization. Throughout the paper, the notation $X_{\text{in}} Y_{\text{out}}$ will be used to define a configuration with incident excitation of polarization X and detection of polarization Y ($X, Y = S$ or P).

The proposed probe design is schematically shown in Fig. 1. The designed probe geometry has the ability to induce a strong antenna dipole response for both p- and s-polarized light. This is due to the addition of a large asymmetrical tail, which enables an increased plasmonic response of the optical antenna in the horizontal direction when s-polarized light is utilized. The large height in the vertical direction still preserves p-polarized scattering efficiency. A tip apex protrusion of height p is added to ensure the tip apex remains as sharp as a regular AFM probe to ensure minimal loss of spatial resolution as well as maximal field enhancing capability. The h , p , and t dimensions of the probe are further optimized utilizing particle swarm optimization to maximize field enhancement factor (FEF)—defined as the electric field halfway between the tip apex and the sample—when illuminated with 1000 cm^{-1} incident light, for both s- and p-polarized incident light to

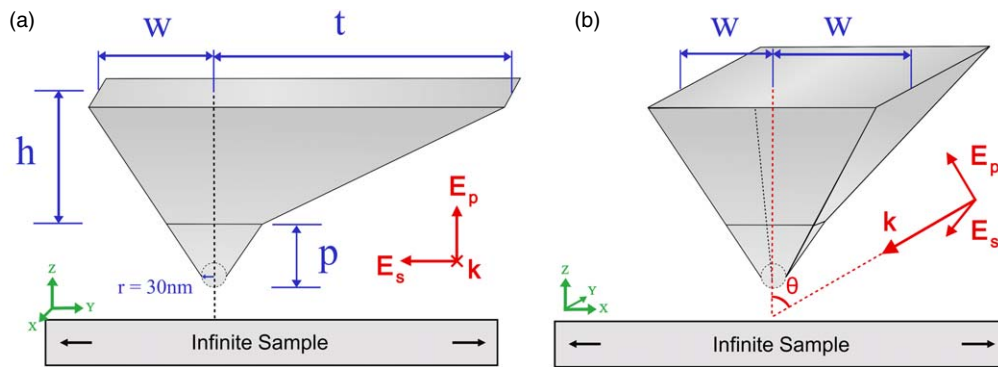


Fig. 1. (Color online) Schematics of the designed probe geometry. (a) Front view and (b) side view of the probe design. The designed probe contains physical extensions in both the horizontal and vertical directions to enhance the dipolar response to different polarizations. The tip apex protrusion enables a small tip apex curvature and high spatial resolution. The final parameter values are $h = 2.5 \mu\text{m}$, $t = 5.2 \mu\text{m}$, $p = 1.9 \mu\text{m}$, and $w = 2.5 \mu\text{m}$. Parameters h , t , and p are optimized utilizing >1000 iterations of particle swarm optimization, while parameter w is specified after optimization (height-dependent) to mimic the conventional probe 45° tip apex. An comparable pyramidal AFM probe with an equivalent height is simulated by setting the pyramidal shaft tail t equal to the pyramidal shaft width w parameter.

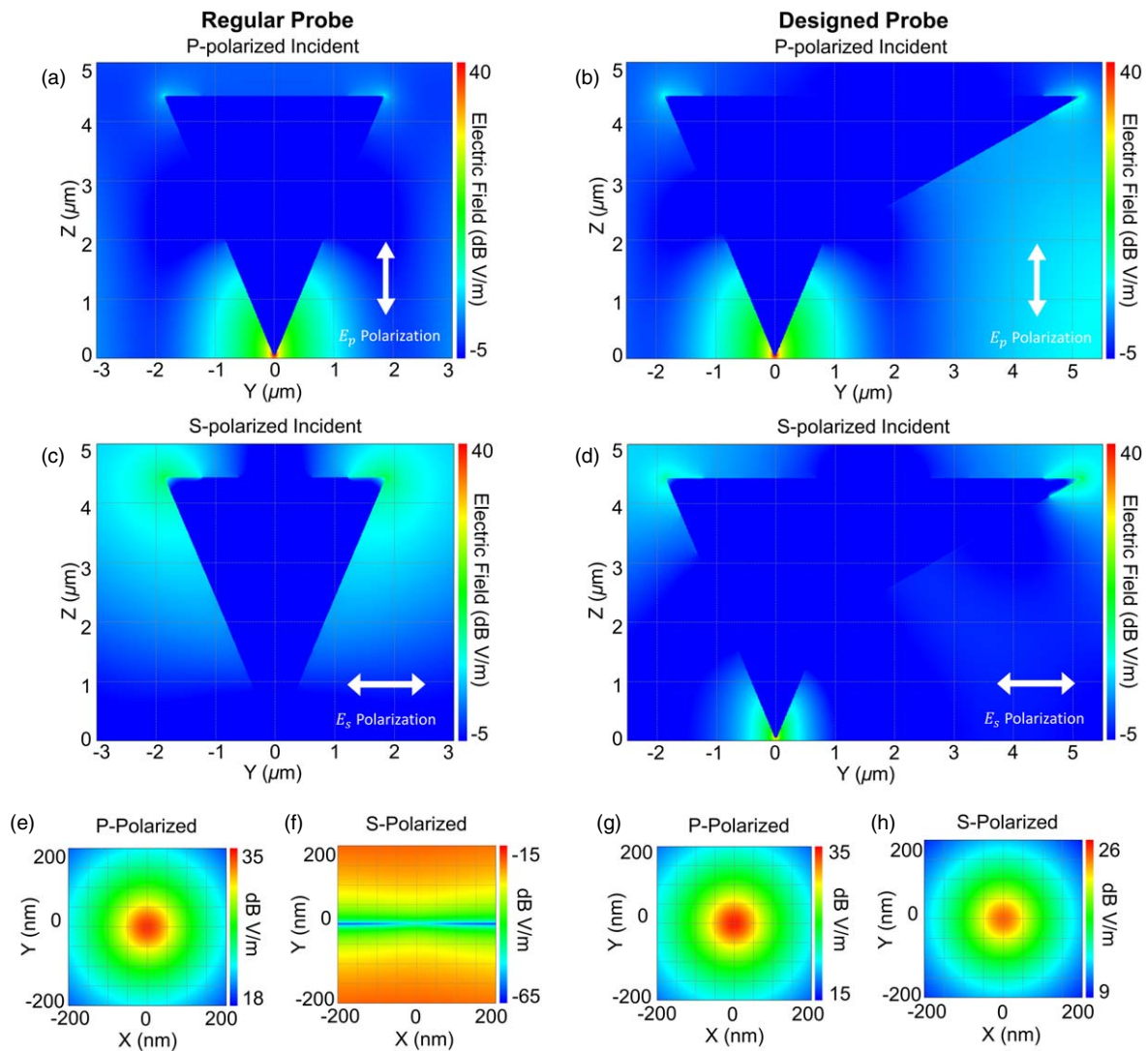


Fig. 2. (Color online) Simulated probe field distribution for P_{in} (a) regular (b) designed and S_{in} (c) regular (d) designed probes. Simulated sample field distribution for regular (e) P_{in} (f) S_{in} and novel (g) P_{in} (h) S_{in} . In response to p-polarized incident light, both the regular probe and designed probe perform similarly, with a 64.428 and 67.143 FEF respectively. In response to s-polarized incident light, the regular probe exhibits very weak field enhancement near the tip apex while the designed probe shows strong field enhancement, with a 21.278 and 0.011 FEF respectively. Sample surface electric field maps show the designed probe does not lose resolution as indicated by the electric field map's perfectly circular enhancement. Probe-sample distance is 50 nm. Sample maps have different electric field scales.

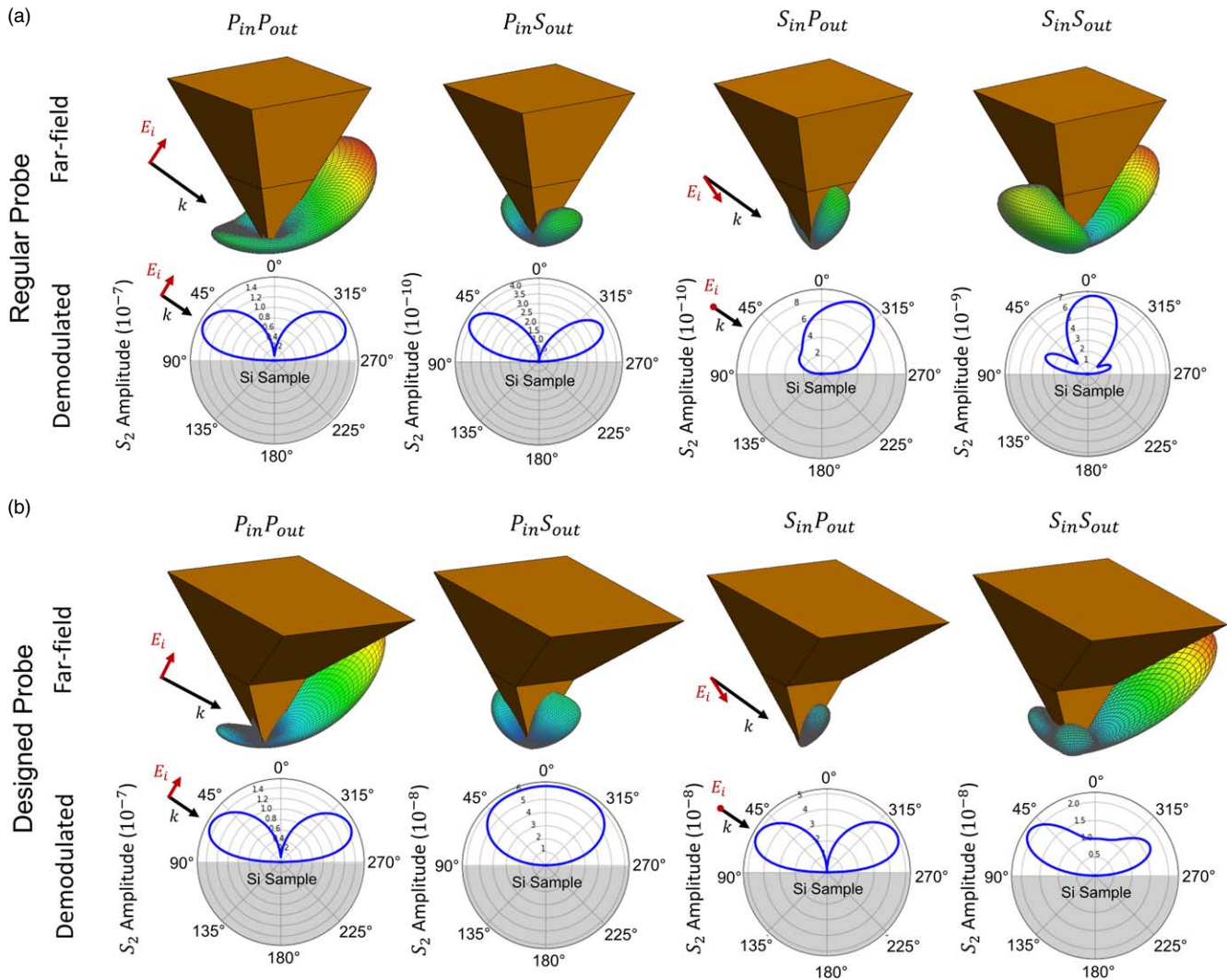


Fig. 3. (Color online) Simulated far-field and demodulated directivity for (a) regular probe and (b) designed probe. The radiation patterns of the probe are simulated in 3D for far-field scattering and plotted across the x - z plane for demodulated scattering amplitude. The tip is in contact with a Si substrate with an incident wavelength of 1000 nm .

ensure optimal efficiency. Throughout this study, a pyramidal AFM probe is simulated in addition to the designed probe in order to provide a quantitative benchmark for comparison. The pyramidal probe is created to mimic commercially available AFM probes such as the PtSi-NCH-50 (NANOSensors, Switzerland).

As an initial antenna response test, the electric field distributions of both probes are simulated. Within the simulations, the sample is set as PEC and the incident wavelength is set to 1000 nm . The probe-sample distance is kept at 50 nm . Furthermore, the FEF was quantified at $z = 25\text{ nm}$ and utilized as a gauge for probe performance. The electric field distributions around the designed and conventional probes are shown in Fig. 2. For p-polarized incident light, both probes show a similar FEF at ~ 60 , which indicates a strong coupling between the probe and sample [Figs. 2(a), 2(b)]. This result is expected because both probes share similar heights, which leads to a comparably dipolar antenna response in the vertical direction. On the contrary, for s-polarized incident light, the response of the designed probe and the conventional probe is drastically distinct. The FEF for the conventional probe is very low while the designed probe successfully enhances the s-polarized light

with an FEF above 20 [Figs. 2(c), 2(d)]. By adding an extension to one side of the AFM probe and optimizing the probe dimensions, we are able to enhance the electric field towards the probe apex. The electric field distributions directly on the sample surface are also simulated to evaluate resolution loss and confirm previous results. The designed probe [Figs. 2(g), 2(h)] retains a similar electric field distribution near the apex to the regular probe for p-polarized [Fig. 2(e)] light. The regular probe, when illuminated with s-polarized incident light, exhibits electric hotspots towards the sides of the probe [Fig. 2(f)].

Simulation of the spectroscopic s-SNOM scattering signal for prototypical materials SiO_2 , SiTrO_3 (STO), and Si are used to quantitatively evaluate the designed and control probes' performance. In the experimental setup of a typical broadband s-SNOM system, an AFM probe harmonically oscillates in tapping mode at its mechanical resonance frequency Ω with a tapping amplitude of $40\text{--}100\text{ nm}$, which results in the modulation of the near-field interaction. Demodulating the scattered signal at higher harmonics of the tip-tapping frequency ($n\Omega$) through a lock-in amplifier eliminates the constant far-field background. The signal is then typically normalized to a material of a constant dielectric

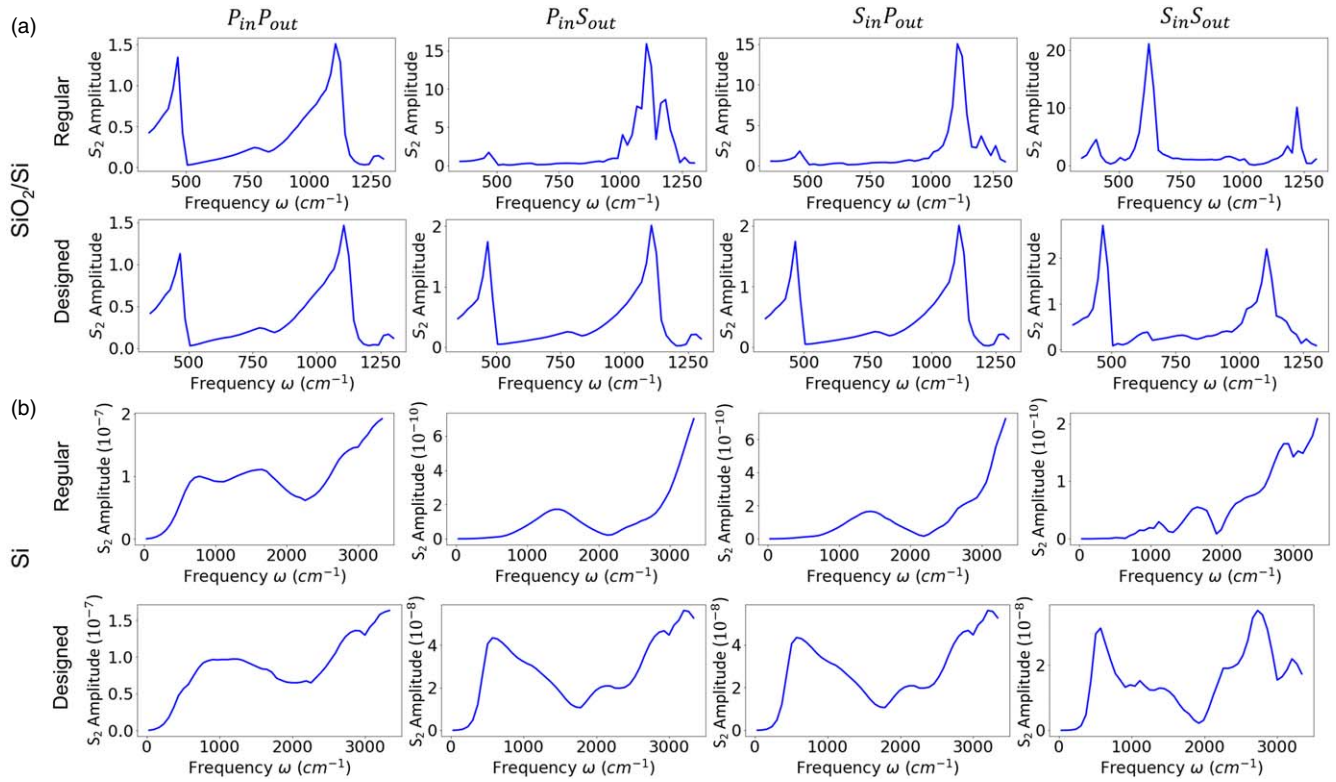


Fig. 4. (Color online) Simulated second harmonic spectra amplitude of (a) SiO₂/Si and (b) Si (unnormalized) for regular and designed probes.

function over the relevant frequency range. In mid-IR, the common reference materials are good metals or intrinsic Si. In the simulations, we aim to fully reproduce these experimental conditions. The far-field scattering is simulated at a series of probe-sample distances given by $z = A - A \cos(\Omega t) + A_0$ for t from 0 to T , where $T = \frac{2\pi}{\Omega}$ is the probe oscillation period. For our simulations, we set the probe-tapping amplitude $A = 50$ nm and minimal probe-sample distance $A_0 = 1$ nm to reflect typical experimental parameters. Simulations are done at either 10 or 15 discretized linearly spaced t points. The complex far-field scattering $f(t)$ is demodulated at 2Ω by $S_2 = s_2 e^{i\phi_2} = \int_0^T f(t) e^{-i2\Omega t} dt$. Finally, the experimental spectrum is normalized to the Si spectrum as $\frac{s_2(\text{exp})}{s_2(\text{Si})}$ and $\phi_2(\text{exp}) - \phi_2(\text{Si})$ to yield quantitatively meaningful values. This process was repeated for both designed and regular probes for the $P_{\text{in}}P_{\text{out}}$, $P_{\text{in}}S_{\text{out}}$, $S_{\text{in}}P_{\text{out}}$, and $S_{\text{in}}S_{\text{out}}$ configurations over a given frequency range with 50 discretized linearly spaced frequency simulation steps.

The scattering from the designed and regular probes exhibits strong angular dependence, influenced by the geometry of the probes. To quantify this dependence, the scattering pattern is simulated for both far-field and near-field scattering (2nd harmonic demodulated signal). As expected, for regular tips, a point-dipole-like optical antenna scattering pattern is obtained with the $P_{\text{in}}P_{\text{out}}$ configuration, with strong scattering peaks near 60° (incident angle) for backscattered detection, and 300° (explementary of incident angle) for forward-scattering detection [Fig. 3(a)]. For the $S_{\text{in}}P_{\text{out}}$ and $S_{\text{in}}S_{\text{out}}$ configurations, on the other hand, regular tips generally exhibit demodulated scattering peaks upward

(0°–45° and 315°–360°). The demodulated radiation patterns for the designed probe show a strong forward-scattering and backscattering for all configurations [Fig. 3(b)]. This further suggests the designed probe has superior near-field performance with s-polarized light.

Next, we investigate the near-field spectroscopic performances of the probes. SiO₂ is a prototypical isotropic material whose near-field response is well known. The demodulated broadband near-field spectra of SiO₂ and Si are simulated with a frequency range of 350–1300 cm^{−1} and a 19 cm^{−1} spectral resolution. The normalized SiO₂ (to Si) spectra are shown in Fig. 4(a). In the $P_{\text{in}}P_{\text{out}}$ scheme, both probes lead to a similar spectrum with clear phonon polariton resonances at ~450 and 1100 cm^{−1} which is consistent with well-known literature results.²¹⁾ However, the spectra alter dramatically when the regular probe incident/detection scheme is changed to include s-polarized light. On the contrary, the designed probe exhibits a very consistent and expected spectra in all polarization schemes. Similar conclusions can be drawn where the sample material is STO and near-field spectra are calculated with a frequency range from 375 to 900 cm^{−1} at a 10.5 cm^{−1} spectral resolution (see supplemental information, available online at stacks.iop.org/APEX/14/022002/mmedia).

To explore why the regular probe is not able to produce meaningful spectra in the $P_{\text{in}}S_{\text{out}}$, $S_{\text{in}}P_{\text{out}}$, and $S_{\text{in}}S_{\text{out}}$ configurations while the designed probe can, in Fig. 4(b) we show the unnormalized broadband near-field amplitude spectra of Si from a frequency range of ~33 to ~3336 cm^{−1}. As indicated by unnormalized spectra, the designed probe exhibits at least two orders of magnitude greater scattering signal in configurations involving s-polarized light compared to the regular probe design.

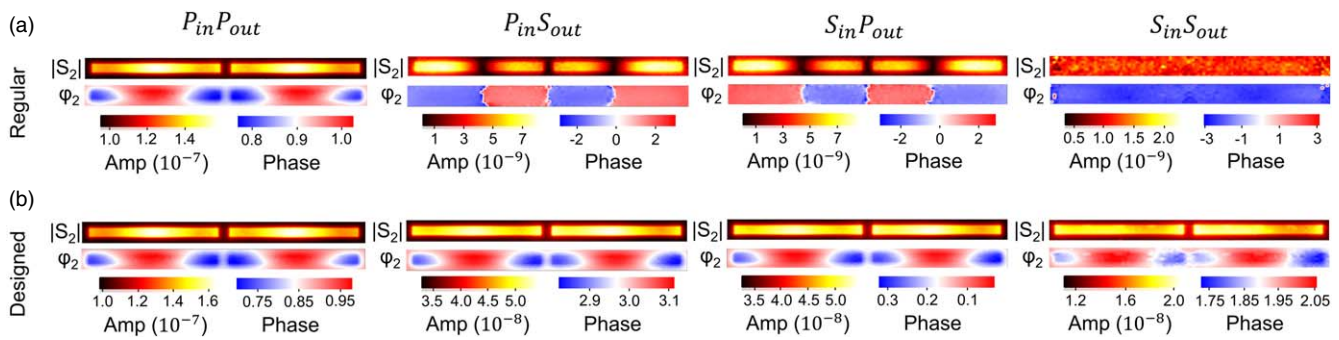


Fig. 5. (Color online) Simulated raster scan of a resonant 2D gap antenna utilizing the (a) regular probe and (b) designed probe. The length of each antenna arm is $2.5\ \mu\text{m}$ and the gap is $200\ \text{nm}$, making the antenna resonant for a $10\ \mu\text{m}$ wavelength.

Besides broadband spectroscopy, monochromatic imaging is equally important and experimentally relevant. Here, we demonstrate simulated s-SNOM imaging on a gap nanoantenna as an example. Two $2.5\ \mu\text{m}$ long 2D rectangular metallic antennas (modeled as PEC) with a $200\ \text{nm}$ gap are utilized as a sample on top of Si substrate. With the incident frequency fixed at $1000\ \text{cm}^{-1}$, the gap antenna is raster-scanned under the probe in steps of $50\ \text{nm}$. The simulation of tip vibration and demodulation is carried out to plot the near-field amplitude and phase. As is evident in Fig. 5, $S_{in}S_{out}$ for normal probes exhibit no discernable signal due to small coupling and scattering cross-section. The designed probe yields similar plasmonic patterns as well as amplitude and phase contrast in the same order of magnitude for all polarization configurations. Amplitude raster scans with $1\ \mu\text{m}$ antenna arms and a $50\ \text{nm}$ gap confirm similar results for non-resonant antennas (see supplemental information).

In summary, the developed high-efficiency probe design highlighted in this paper will enable s-SNOM to measure anisotropic optical properties in both the out-of-plane and in-plane direction without losing spatial resolution and signal strength. These developments could help to locate signatures of polarization-dependent and/or anisotropic sample properties in photonic and biological samples at the nanoscale. Many material properties, such as in-plane phonons or excitons, require interaction with s-polarized light, especially in 2D materials. Previous examination of barium titanite, SrTiO_3 , LiNbO_3 , and $\text{PbZr}_{0.2}\text{Ti}_{0.8}\text{O}_3$, Ag nanowires, and cancerous tissues further indicate the importance of in-plane surface plasmon resonances in imaging and nanoengineering.^{22–27}

Previous studies have also indicated the need for a circularly-polarized light scattering probe design.²⁸ Since circularly-polarized light is a vectorial combination of p- and s-polarized light, this probe design may enable the measurement of spin chirality and near-field circular dichroism at a nanoscale resolution, proving useful to the testing of chiral systems including topological materials, metamaterials, and chiral photonic devices.^{29–31} The potential for circular dichroism measurements with this probe design can be further investigated in future studies.

Acknowledgments We would like to acknowledge support from the National Science Foundation under grant no. DMR-1904576. This work was partly supported by the RISE2 node of NASA's Solar System Exploration Research Virtual Institute under NASA Cooperative Agreement 80NSSC19MO2015. We would also like to thank Derek Chen, Patrick McArdle, and Prof. Mumtaz Qazilbash for their assistance with the Altair FEKO method-of-moments simulation software.

ORCID iDs Richard Ren  <https://orcid.org/0000-0001-5628-7926> Xinzhong Chen  <https://orcid.org/0000-0002-6103-3848>

- 1) X. Chen, D. Hu, R. Mescall, G. You, D. N. Basov, Q. Dai, and M. Liu, *Adv. Mater.* **31**, 1804774 (2019).
- 2) J. M. Atkin, S. Berweger, A. C. Jones, and M. B. Raschke, *Adv. Phys.* **61**, 745 (2012).
- 3) S. Mastel, M. B. Lundeberg, P. Alonso-González, Y. Gao, K. Watanabe, T. Taniguchi, J. Hone, F. H. L. Koppens, A. Y. Nikitin, and R. Hillenbrand, *Nano Lett.* **17**, 6526 (2017).
- 4) A. Hartschuh, *Angew. Chem.—Int. Ed.* **47**, 8178 (2008).
- 5) F. Keilmann and R. Hillenbrand, *Phil. Trans. A* **362**, 787 (2004).
- 6) T. Neuman, P. Alonso-González, A. Garcia-Etxarri, M. Schnell, R. Hillenbrand, and J. Aizpurua, *Laser Photonics Rev.* **9**, 637 (2015).
- 7) R. L. Olmon, P. M. Krenz, A. C. Jones, G. D. Boreman, and M. B. Raschke, *Opt. Express* **16**, 20295 (2008).
- 8) J. D' Archangel, E. Tucker, E. Kinzel, E. A. Muller, H. A. Bechtel, M. C. Martin, M. B. Raschke, and G. Boreman, *Opt. Express* **21**, 17150 (2013).
- 9) B. Knoll and F. Keilmann, *Opt. Commun.* **182**, 321 (2000).
- 10) A. Cvitkovic, N. Ocelic, and R. Hillenbrand, *Opt. Express* **15**, 8550 (2007).
- 11) A. S. McLeod, P. Kelly, M. D. Goldflam, Z. Gainsforth, A. J. Westphal, G. Dominguez, M. H. Thiemens, M. M. Fogler, and D. N. Basov, *Phys. Rev. B* **90**, 085136 (2014).
- 12) B.-Y. Jiang, L. M. Zhang, A. H. Castro Neto, D. N. Basov, and M. M. Fogler, *J. Appl. Phys.* **119**, 054305 (2016).
- 13) S. T. Chui, M. Liu, X. Chen, Z. Lin, and J. Zi, *Phys. Rev. B* **97**, 081406 (2018).
- 14) X. Chen, C. F. B. Lo, W. Zheng, H. Hu, Q. Dai, and M. Liu, *Appl. Phys. Lett.* **111**, 223110 (2017).
- 15) F. Mooshammer, M. A. Huber, F. Sandner, M. Plankl, M. Zizlsperger, and R. Huber, *ACS Photonics* **7**, 344 (2020).
- 16) Y. Luan, L. McDermott, F. Hu, and Z. Fei, *Phys. Rev. Appl.* **13**, 034020 (2020).
- 17) C. Maissen, S. Chen, E. Nikulina, A. Govyadinov, and R. Hillenbrand, *ACS Photonics* **6**, 1279 (2019).
- 18) W. C. Gibson, *The Method of Moments in Electromagnetics* (CRC Press, Boca Raton, FL, 2007).
- 19) E. H. Newman and K. Kingsley, *Comput. Phys. Commun.* **68**, 1 (1991).
- 20) P. McArdle, D. J. Lahnenman, A. Biswas, F. Keilmann, and M. M. Qazilbash, *Phys. Rev. Res.* **2**, 023272 (2020).
- 21) L. M. Zhang, G. O. Andreev, Z. Fei, A. S. McLeod, G. Dominguez, M. Thiemens, A. H. Castro-Neto, D. N. Basov, and M. M. Fogler, *Phys. Rev. B* **85**, 075419 (2012).
- 22) S. C. Schneider, S. Grafström, and L. M. Eng, *Phys. Rev. B* **71**, 115418 (2005).
- 23) L. Wehmeier, D. Lang, Y. Liu, X. Zhang, S. Winnerl, L. M. Eng, and S. C. Kehr, *Phys. Rev. B* **100**, 035444 (2019).
- 24) M. Yang, W. Cai, Y. Wang, M. Sun, and G. Shang, *Sci. Rep.* **6**, 25633 (2016).
- 25) H. Wang, T. Akkin, C. Magnain, R. Wang, J. Dubb, W. J. Kostis, M. A. Yaseen, A. Cramer, S. Sakadžić, and D. Boas, *Opt. Lett.* **41**, 2213 (2016).
- 26) F. A. South, E. J. Chaney, M. Marjanovic, S. G. Adie, and S. A. Boppart, *Biomed. Opt. Express* **5**, 3417 (2014).
- 27) E. Götzinger, M. Pircher, M. Sticker, A. F. Fercher, and C. K. Hitzengerger, *J. Biomed. Opt.* **9**, 94 (2004).
- 28) T. Ishibashi and Y. Cai, *Nanoscale Res. Lett.* **10**, 375 (2015).
- 29) Y. Liu, G. Bian, T. Miller, and T. C. Chiang, *Phys. Rev. Lett.* **107**, 166803 (2011).
- 30) F. Liang, B. L. Gao, Y. Gu, and C. Yang, *Chin. Phys. Lett.* **33**, 047201 (2016).
- 31) M. Schnell, P. Sarriugarte, T. Neuman, A. B. Khanikaev, G. Shvets, J. Aizpurua, and R. Hillenbrand, *Nano Lett.* **16**, 663 (2016).